

# QCD Tests at HERA<sup>†</sup>

C Glasman<sup>a\*</sup>  
 representing the H1 and ZEUS Collaborations

<sup>a</sup> Departamento de Física Teórica, Universidad Autónoma de Madrid,  
 Cantoblanco, 28049 Madrid, Spain  
 E-mail: [claudia@mail.desy.de](mailto:claudia@mail.desy.de)

## Abstract

Measurements of inclusive jet, dijet and three-jet cross sections in photon-proton interactions are presented. These measurements provide new tests of QCD, constrain the parton densities of the photon, and allow searches for new physics. Measurements of the mean subjet multiplicity are reported and used to test the differences between quark and gluon jets.

## 1. Introduction

Measurements of cross sections for processes involving a large momentum transfer (e.g. jets in  $\gamma p$  interactions) are compared to next-to-leading order (NLO) calculations to test QCD. These measurements also provide a test of the parametrisations of the photon parton densities and may be used in global analyses to constrain the parton distributions.

The investigation of the internal structure of jets gives insight into the transition between a parton produced in a hard process and the experimentally observable spray of hadrons. Measurements of jet substructure allow the study of the characteristics of quark and gluon jets.

## 2. Jet cross sections in $\gamma p$ interactions

At HERA, positrons of energy  $E_e = 27.5$  GeV collide with protons of energy  $E_p = 820$  GeV. The main source of jets at HERA is hard scattering in  $\gamma p$  interactions in which a quasi-real photon ( $Q^2 \approx 0$ , where  $Q^2$  is the virtuality of the photon) emitted by the positron beam interacts with a parton from the proton to produce two jets in the final state. At leading order (LO) QCD, there are two processes which contribute to the jet production cross section: the resolved process (figure 1a) in which the photon interacts through its partonic

content, and the direct process (figure 1b) in which the photon interacts as a point-like particle.

The cross section for jet production at LO QCD in  $\gamma p$  interactions is given by

$$\sigma_{\text{direct}}^{\text{LO}, \text{ep} \rightarrow 2\text{jet}} = \int d\Omega f_{\gamma/e}(y) f_{j/p}(x_p, \mu_F^2) \times d\sigma(\gamma j \rightarrow \text{jet jet})$$

and

$$\sigma_{\text{resolved}}^{\text{LO}, \text{ep} \rightarrow 2\text{jet}} = \int d\Omega f_{\gamma/e}(y) f_{j/p}(x_p, \mu_F^2) \times f_{i/\gamma}(x_\gamma, \mu_F^2) d\sigma(i j \rightarrow \text{jet jet}),$$

where  $f_{\gamma/e}(y)$  is the flux of photons in the positron, usually estimated by the Weizsäcker-Williams approximation [1] ( $y$  is the fraction of the positron energy taken by the photon);  $f_{j/p}(x_p, \mu_F^2)$  are the parton densities in the proton, determined from e.g. global fits [2] ( $x_p$  is the fraction of the proton momentum taken by parton  $j$  and  $\mu_F$  is the factorisation scale); and  $d\sigma(i j \rightarrow \text{jet jet})$  is the subprocess cross section, calculable in perturbative QCD. In the case of resolved processes, there is an additional ingredient:  $f_{i/\gamma}(x_\gamma, \mu_F^2)$  are the parton densities in the photon, for which there is only partial information ( $x_\gamma$  is the fraction of the photon momentum taken by parton  $i$ ). The integrals are performed over the phase space represented by “ $d\Omega$ ”.

### 2.1. The iterative cone algorithm

In hadronic type interactions, jets are usually reconstructed by a cone algorithm [3]. Experimentally, jets are found in the pseudorapidity ( $\eta$ ) – azimuth ( $\varphi$ ) plane using the transverse energy flow of the

<sup>†</sup> Talk given at the *International Europhysics Conference on High Energy Physics*, Tampere, Finland, July 15<sup>th</sup> – 21<sup>th</sup>, 1999.

<sup>\*</sup> Supported by an EC fellowship number ERBFMBICT 972523.

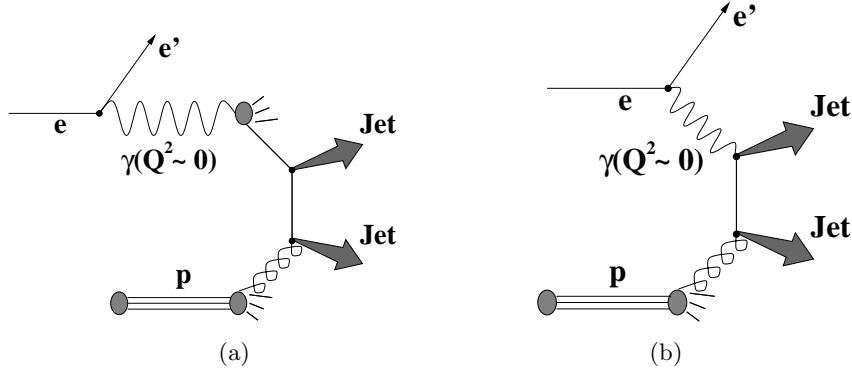


**Figure 1.** (a) Resolved- and (b) direct-photon processes.

event. The jet variables are defined according to the Snowmass Convention [4],

$$E_T^{jet} = \sum_i E_T^i$$

$$\eta^{jet} = \frac{\sum_i E_T^i \cdot \eta_i}{E_T^{jet}}; \quad \varphi^{jet} = \frac{\sum_i E_T^i \cdot \varphi_i}{E_T^{jet}}.$$

In the iterative cone algorithm, jets are found by maximising the summed transverse energy within a cone of radius  $R$ .

### 3. Inclusive jet cross sections

Inclusive jet cross sections have been measured [5] using the 1995–1997 ZEUS [6] data (which amounts to an integrated luminosity of  $\mathcal{L} \sim 43 \text{ pb}^{-1}$ ) as a function of the jet transverse energy. The jets have been searched for with an iterative cone algorithm with  $R = 1$ . The measurements have been performed for jets of hadrons with  $E_T^{jet}$  between 17 and 74 GeV and  $\eta^{jet}$  between  $-0.75$  and  $2.5$ , and are given for the kinematic region defined by  $0.2 < y < 0.85$  and  $Q^2 \leq 4 \text{ GeV}^2$ .

Figure 2a shows the measured  $d\sigma/dE_T^{jet}$  (black dots). The systematic uncertainties not associated with the absolute energy scale of the jets have been added in quadrature to the statistical errors (thick error bars) and are shown as thin error bars. The shaded band represents the uncertainty on the energy scale of the jets. The data show a steep fall-off over four orders of magnitude in the measured range.

#### 3.1. NLO QCD calculations

There are several complete calculations of jet cross sections at NLO for  $\gamma p$  interactions [7, 8, 9, 10]. Two types of corrections contribute at NLO: the virtual corrections which include internal particle loops and the real corrections which include a third parton in the final state. The existing calculations differ

mainly in the treatment of the real corrections. A detailed comparison of the calculations [11] show that for NLO calculations of dijet cross sections and LO calculations of three-jet cross sections a reasonable agreement is found, and the differences are up to  $\sim 5\%$ .

The curves in figure 2a are NLO QCD calculations [7, 8] using different parametrisations of the photon structure function: GS96 [12] (solid line), GRV-HO [13] (dashed line) and AFG [14] (dot-dashed line). The CTEQ4M [15] proton parton densities have been used in all cases. In the calculations shown here, the renormalisation and factorisation scales have been chosen equal to  $E_T^{jet}$  and  $\alpha_s$  was calculated at 2-loops with  $\Lambda_{\overline{MS}}^{(4)} = 296 \text{ MeV}$ . The NLO calculations give a reasonable description of the data. Figure 2b shows the fractional differences between the measured  $d\sigma/dE_T^{jet}$  and the NLO calculations based on GRV-HO.

#### 3.2. Comparing theory and experiment

To perform tests of QCD and to extract information on the photon parton densities, the experimental and theoretical uncertainties must be reduced as much as possible.

Among the main experimental uncertainties the presence of a possible underlying event, which is the result of soft interactions between the partons in the photon and proton remnants (for resolved events), and is not included in the calculations. The uncertainty of the measurements due to the underlying event is reduced by decreasing the cone radius or by increasing the transverse energy of the jets [16].

On the theoretical side, since calculations are made only at NLO, the implementation of the iterative cone jet algorithm in the theory does not match the experimental procedure exactly. The theoretical uncertainty coming from this effect is

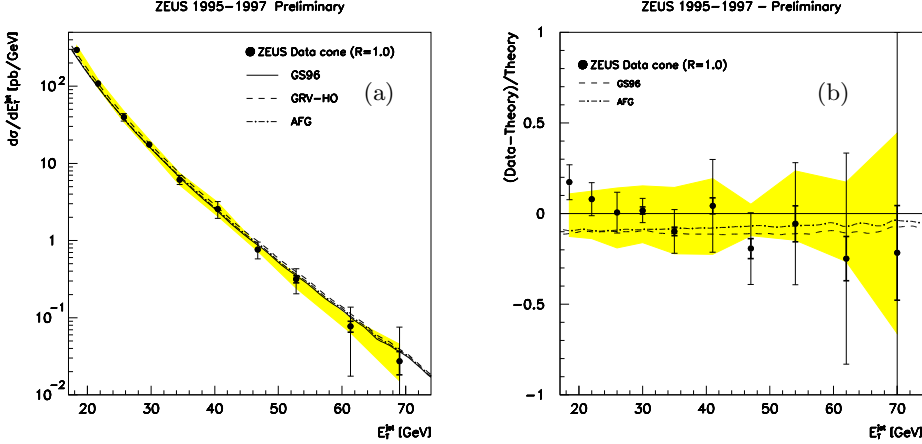


**Figure 2.** Inclusive jet cross section as a function of  $E_T^{jet}$  using the iterative cone algorithm. NLO QCD calculations are shown for comparison.

reduced by using the longitudinally invariant  $k_T$  cluster algorithm [17].

### 3.3. The $k_T$ cluster algorithm

In the inclusive  $k_T$  cluster algorithm [17], jets are identified by successively combining nearby pairs of particles until a jet is complete. The  $k_T$  algorithm allows a transparent translation of the theoretical jet algorithm to the experimental set-up by avoiding the ambiguities related to the merging and overlapping of jets and it is infrared safe to all orders.

Figure 3 shows  $d\sigma/dE_T^{jet}$  for jets found using the  $k_T$  cluster algorithm. The NLO QCD calculations, using the current knowledge of the photon structure, are able to describe the data within the present experimental and theoretical uncertainties.

A comparison between  $d\sigma/dE_T^{jet}$  measured using the cone and the  $k_T$  algorithms has been made (see figure 4). The differences between the measured cross sections are typically smaller than 10%. This comparison shows that the cone with  $R = 1$  and the  $k_T$  cluster algorithms probe the underlying parton dynamics in a comparable way. Therefore, in the experiment, the choice of jet algorithm is not crucial. The use of the  $k_T$  cluster algorithm is dictated by the need to reduce the theoretical uncertainties.

## 4. Jet substructure

The use of the  $k_T$  cluster algorithm allows the study of the internal structure of the jets in terms of subjets. Subjets are jet-like objects within a jet and are resolved by reapplying the  $k_T$  cluster algorithm until for every pair of particles  $i$  and  $j$ ,

$$\begin{aligned} d_{ij} &= \min(E_{Ti}, E_{Tj})^2[(\eta_i - \eta_j)^2 + (\varphi_i - \varphi_j)^2] \\ &\geq y_{\text{cut}}(E_T^{jet})^2. \end{aligned}$$

Measurements of the mean subjet multiplicity ( $\langle n_{\text{subjet}} \rangle$ ) have been performed by ZEUS [18] using an inclusive sample of jets with  $E_T^{jet} > 15$  GeV and  $-1 < \eta^{jet} < 2$  in the kinematic range defined by  $0.2 < y < 0.85$  and  $Q^2 \leq 1$  GeV $^2$ .

Figure 5a shows  $\langle n_{\text{subjet}} \rangle$  as a function of  $y_{\text{cut}}$ . The data (black dots, the statistical and systematic uncertainties are included but are smaller than the dots) show that  $\langle n_{\text{subjet}} \rangle$  grows as  $y_{\text{cut}}$  decreases within the measured range. The lines are calculations from the leading-logarithm parton-shower Monte Carlo's PYTHIA [19] and HERWIG [20]. The calculations based on PYTHIA give a good description of the data. Figure 5b shows  $\langle n_{\text{subjet}} \rangle$  as a function of  $\eta^{jet}$  for  $y_{\text{cut}} = 0.01$ :  $\langle n_{\text{subjet}} \rangle$  increases as  $\eta^{jet}$  increases. The comparison with the predictions for quark and gluon jets shows that the increase in  $\langle n_{\text{subjet}} \rangle$  as  $\eta^{jet}$  increases is consistent with the predicted increase in the fraction of gluon jets.

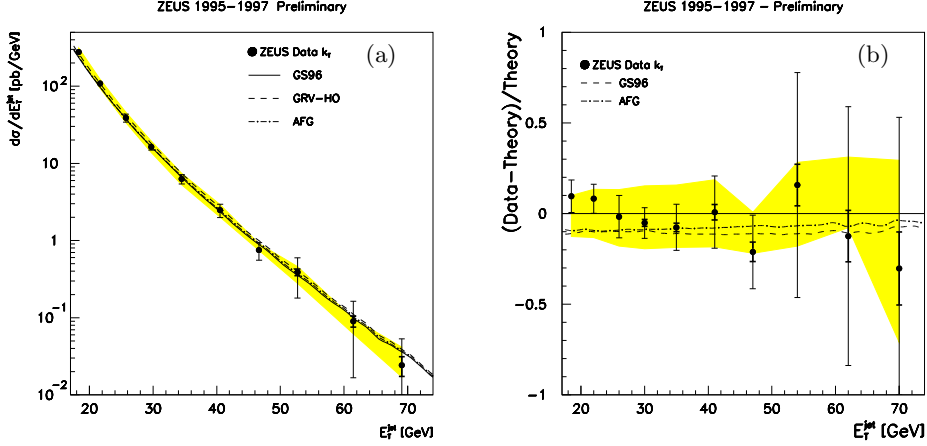


**Figure 3.** Inclusive jet cross section as a function of  $E_T^{jet}$  using the  $k_T$  cluster algorithm. NLO QCD calculations are shown for comparison.

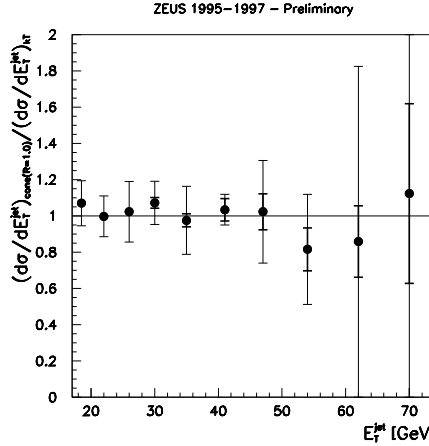


**Figure 4.** Ratio between the measured  $d\sigma/dE_T^{jet}$  using the iterative cone and the  $k_T$  cluster algorithms.

## 5. Dijet cross sections

Dijet cross sections have been measured [21] using the 1994 – 1997 H1 [22] data (which amounts to an integrated luminosity of  $\mathcal{L} \sim 36 \text{ pb}^{-1}$ ) as a function of the transverse energy of the leading jet and the average transverse energy of the two leading jets. The jets have been found using the  $k_T$  cluster algorithm. The measurements have been performed for jets of hadrons with  $E_T^{jet1} > 25 \text{ GeV}$ ,  $E_T^{jet2} > 15 \text{ GeV}$  and  $-0.5 < \eta^{jet} < 2.5$ , and are given for the kinematic region defined by  $y < 0.9$  and  $Q^2 < 4 \text{ GeV}^2$ .

Figure 6 shows the measured cross sections (black dots). The systematic uncertainties (including that associated with the absolute energy scale of the jets) have been added in quadrature to the statistical errors (inner error bars) and are shown as the outer error bars. The data show a steep fall-off of three orders of magnitude in the measured range. The histograms are the calculations using PYTHIA which provide a good description of the shape of the measured distributions.

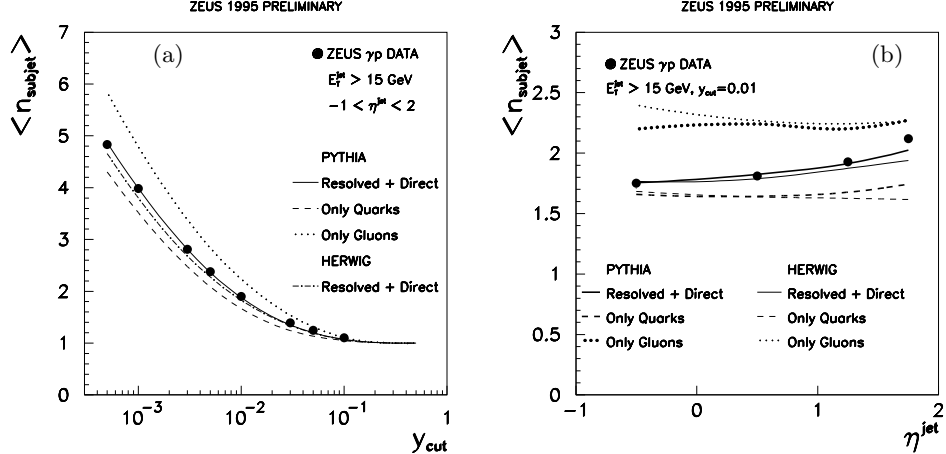


**Figure 5.** Mean subject multiplicity as a function of (a)  $y_{\text{cut}}$  for  $-1 < \eta^{\text{jet}} < 2$  and (b)  $\eta^{\text{jet}}$  for  $y_{\text{cut}} = 0.01$ . PYTHIA and HERWIG Monte Carlo calculations are shown for comparison.

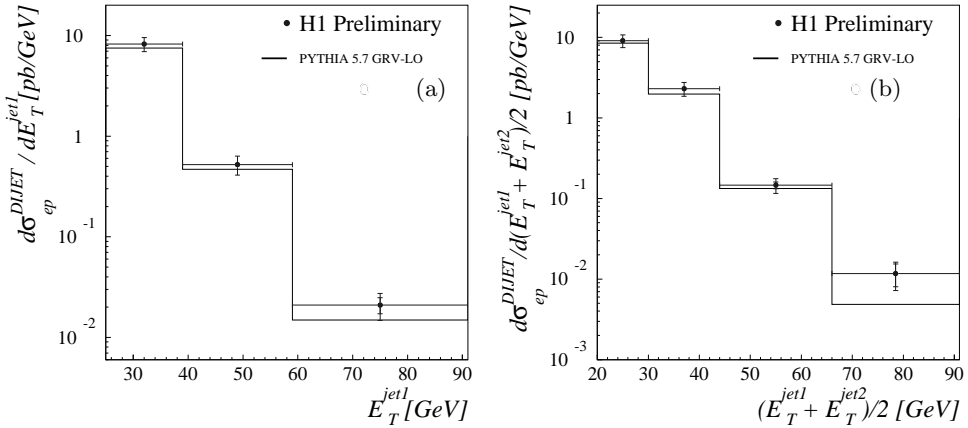


**Figure 6.** Dijet cross sections as a function of (a) the transverse energy of the leading jet and (b) the average transverse energy of the two leading jets. PYTHIA Monte Carlo calculations are shown for comparison.

## 6. High-mass dijet cross sections

The dijet mass distribution  $M^{JJ}$  is sensitive to the presence of new particles or resonances that decay into two jets. The distribution of the angle between the jet-jet axis and the beam direction in the dijet centre-of-mass system ( $\cos\theta^*$ ) reflects the underlying parton dynamics and is sensitive to the spin of the exchanged particle. New particles or resonances decaying into two jets may also be identified by deviations in the measured  $\cos\theta^*$  distribution with respect to the QCD predictions.

The cross section as a function of the dijet invariant mass has been measured by H1 [21] using

the  $k_T$  cluster algorithm between 48 and 148 GeV (figure 7). The data show a steep fall off of more than two orders of magnitude within the measured range. The histogram is the calculation using PYTHIA which gives a reasonable description of the shape of the measured distribution. There are large uncertainties in the normalisation of the LO QCD calculations which indicate the need for NLO corrections.

High-mass dijet cross sections have been measured [23] using the 1995 – 1997 ZEUS data as a function of  $M^{JJ}$  and  $|\cos\theta^*|$ . The measurements have been performed for  $M^{JJ} > 47 \text{ GeV}$  and

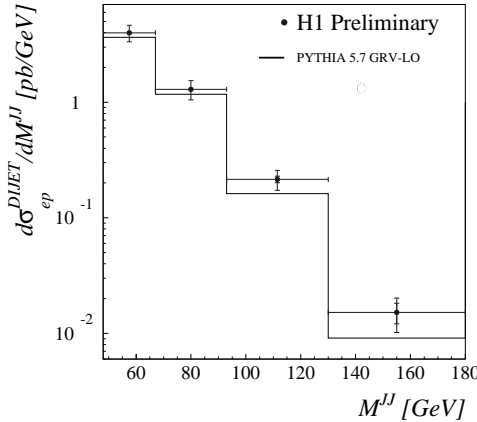


**Figure 7.** Dijet cross section as a function of the dijet invariant mass. PYTHIA Monte Carlo calculations are shown for comparison.

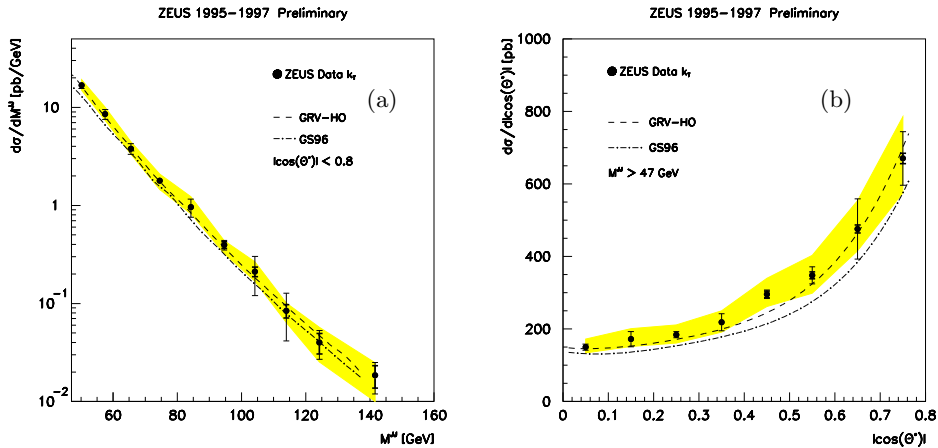


**Figure 8.** High-mass dijet cross sections as a function of (a) the dijet invariant mass and (b) the dijet angular distribution. NLO QCD calculations are shown for comparison.

$|\cos \theta^*| < 0.8$  using the  $k_T$  cluster algorithm.

The data show a steep fall-off in  $M^{JJ}$  of three orders of magnitude in the measured range (figure 8a). The measured  $d\sigma/d|\cos \theta^*|$  rises as  $|\cos \theta^*|$  increases (figure 8b). The NLO QCD calculations [7] give a reasonable description of the measured distributions. The calculations based on GRV-HO are closer in magnitude to the measured cross sections. No significant deviation between data and NLO calculations is observed in the measured range of  $M^{JJ}$  and  $|\cos \theta^*|$ .

## 7. Three-jet cross sections

Measurements of three-jet cross sections provide a test of QCD beyond LO and allow a search for new phenomena. NLO calculations for three-jet cross sections in  $\gamma p$  interactions are not yet available. The calculations shown here are LO for these processes and are therefore subject to large renormalisation and factorisation scale uncertainties. The cross section for three-jet production at LO is given by

$$\sigma_{\text{dir [res]}}^{LO, ep \rightarrow 3\text{jet}} = \int d\Omega \ f_{\gamma/e}(y) \ f_{j/p}(x_p, \mu_F^2) \times [f_{i/\gamma}(x_\gamma, \mu_F^2)] \ d\sigma(\gamma[i]j \rightarrow \text{jet jet jet}).$$

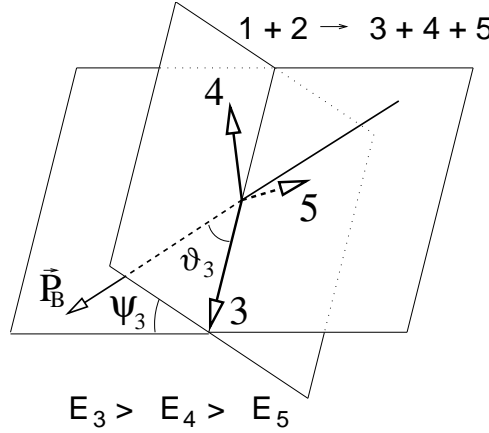


Figure 9. Three-body rest frame.

Five parameters are necessary to uniquely determine the three-body phase-space. These are the three-jet invariant mass ( $M_{3j}$ ); the energy-sharing quantities  $X_3$  and  $X_4$  (the jets are numbered 3, 4 and 5 in order of decreasing energy),

$$X_i \equiv \frac{2E_i}{M_{3j}};$$

the cosine of the scattering angle of the highest energy jet with respect to the beam,

$$\cos \theta_3 \equiv \frac{\vec{p}_B \cdot \vec{p}_3}{|\vec{p}_B||\vec{p}_3|};$$

and  $\psi_3$ , the angle between the plane containing the highest energy jet and the beam and the plane containing the three jets. The latter is defined by

$$\cos \psi_3 \equiv \frac{(\vec{p}_3 \times \vec{p}_B) \cdot (\vec{p}_4 \times \vec{p}_5)}{|\vec{p}_3 \times \vec{p}_B||\vec{p}_4 \times \vec{p}_5|}.$$

The definition of the angles  $\theta_3$  and  $\psi_3$  is illustrated in figure 9.

Since  $\theta_3$  involves only the highest energy jet, the distribution of  $\cos \theta_3$  in three-jet events is expected to follow closely the distribution of  $\cos \theta^*$  in dijet events. The  $\psi_3$  angle, on the other hand, reflects the orientation of the lowest energy jet.

Figure 10 shows the three-jet cross section as a function of the transverse energy of the lowest energy jet and the three-jet invariant mass. The comparison to the calculations using PYTHIA Monte Carlo shows that the parton shower models describe the shape of the measured cross sections.

The three-jet invariant mass cross section was measured by ZEUS [24] in the kinematic region defined by  $|\cos \theta_3| < 0.8$  and  $X_3 < 0.95$  (see figure 11). The curves in figure 11 are the  $\mathcal{O}(\alpha \alpha_s^2)$  QCD calculations [25, 26] using the GRV-LO [13] parametrisations of the photon structure function and the CTEQ4 LO [15] proton parton densities. The renormalisation and factorisation scales have been chosen equal to  $E_T^{\max}$ , the largest of the  $E_T^{\text{jet}}$

values of the three jets.  $\alpha_s$  was calculated at 1-loop with  $\Lambda_{\overline{\text{MS}}}^{(5)} = 181$  MeV. The calculations give a good description of the data, even though they are LO for this process. Monte Carlo calculations are also compared to the data: they provide a good description of the data in shape, but the magnitude is 30–40% too low.

The search for new particles or resonances decaying into two jets can be extended by looking for deviations in the distributions of the dijet invariant masses in three-jet events with respect to the predictions of QCD. Figure 12 shows the dijet invariant mass distributions in three-jet events for all possible pairs of jets. The histograms are the predictions from the QCD-based Monte Carlo models. No significant deviation between data and calculations is observed up to the highest invariant mass value studied.

Figure 13a and 13b show the  $X_3$  and  $X_4$  distributions measured by ZEUS [24] for  $M_{3j} > 50$  GeV,  $|\cos \theta_3| < 0.8$  and  $X_3 < 0.95$ . Calculations from different models are compared to the data: a pure phase space calculation does not describe the data. The  $\mathcal{O}(\alpha \alpha_s^2)$  QCD calculations are in good agreement with the data.

The angular distribution of the lowest energy jet in three-jet events is a distinct probe of the dynamics beyond LO. The measured  $\psi_3$  distribution (figure 13d) is drastically different from pure phase space and is in agreement with the  $\mathcal{O}(\alpha \alpha_s^2)$  QCD calculations. The comparison of the data to parton shower models shows that the data favour color coherence.

The measured  $\cos \theta_3$  distribution [27] (figure 13c) indicates that the highest energy jet tends to go either forward (proton direction) or towards the rear (photon direction). The  $\mathcal{O}(\alpha \alpha_s^2)$  QCD calculations and the Monte Carlo models are in good agreement with the data.

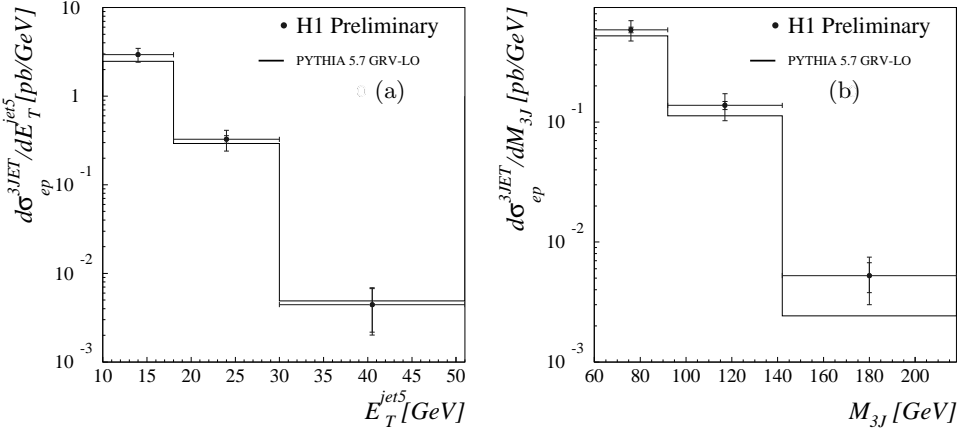


**Figure 10.** Three-jet cross section as a function of (a) the transverse energy of the lowest-energy jet and (b) the three-jet invariant mass. PYTHIA Monte Carlo calculations are shown for comparison.

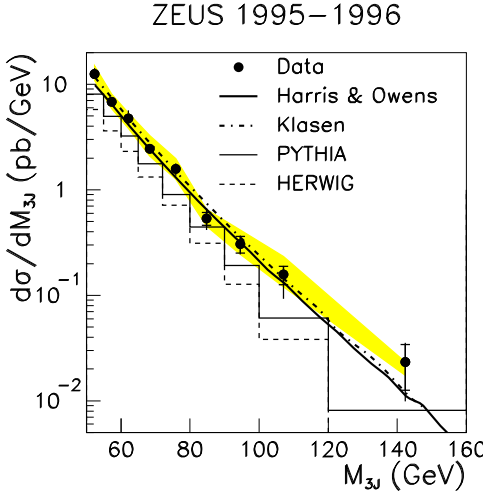


**Figure 11.** Three-jet invariant mass cross section.  $\mathcal{O}(\alpha\alpha_s^2)$  and Monte Carlo calculations are shown for comparison.

The variable  $x_\gamma^{OBS}$ ,

$$x_\gamma^{OBS} \equiv \frac{\sum_{jets} E_T^{jet} e^{-\eta^{jet}}}{2yE_e}$$

gives the fraction of the photon energy invested in the production of the three-jet system and can be used to define resolved and direct processes in a meaningful way to all orders.

Figure 14 shows the  $\cos\theta_3$  distribution for different regions of  $x_\gamma^{OBS}$ . The data indicate that the highest energy jet tends to go in the forward direction for  $x_\gamma^{OBS} < 0.5$  (where LO resolved processes dominate) and it goes more backward as

$x_\gamma^{OBS}$  increases. The  $\mathcal{O}(\alpha\alpha_s^2)$  QCD calculations are in good agreement with the data except for  $0.9 < x_\gamma^{OBS} < 1$ .

## 8. Conclusions

Significant progress in comparing measurements and QCD calculations of jet cross sections in  $\gamma p$  interactions has been achieved; experimental and theoretical uncertainties have been reduced.

NLO QCD calculations of inclusive jet and dijet cross sections and  $\mathcal{O}(\alpha\alpha_s^2)$  QCD calculations of three-jet cross sections describe reasonably well

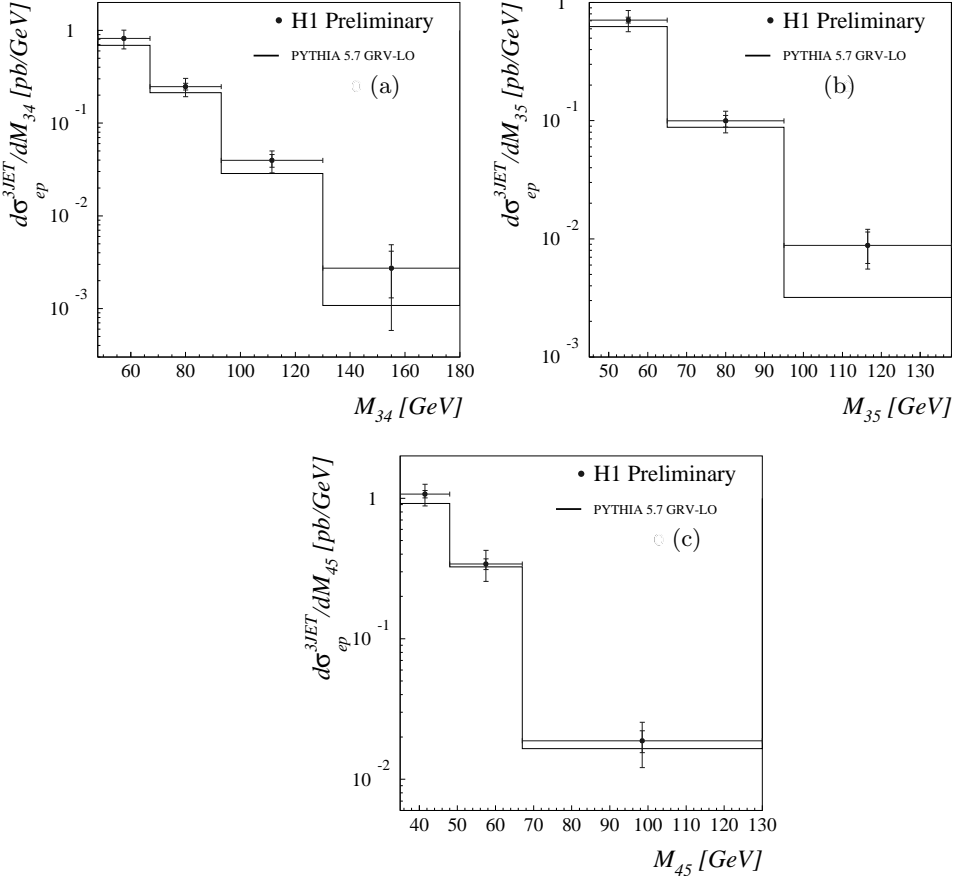


**Figure 12.** Dijet invariant mass cross sections in three-jet events. PYTHIA Monte Carlo calculations are shown for comparison.

the measurements. No significant deviation with respect to QCD predictions has been observed within the measured range of the variables studied.

### Acknowledgements

I would like to thank my colleagues from H1 and ZEUS for their help in preparing this report.

### References

- [1] C.F.v. Weizsäcker, *Z. Phys.* **88** (1934) 612; E.J. Williams, *Phys. Rev.* **45** (1934) 729.
- [2] A.D. Martin, R.G. Roberts, W.J. Stirling and R.S. Thorne, hep-ph/9805205; M. Glück, E. Reya and A. Vogt, *Z. Phys. C* **67** (1995) 433; CTEQ Collab., H.L. Lai *et al.*, hep-ph/9903282.
- [3] CDF Collab., F. Abe *et al.*, *Phys. Rev. D* **45** (1992) 1448.
- [4] J. Huth *et al.*, Proc. of the 1990 DPF Summer Study on High Energy Physics, Snowmass, Colorado, edited by E.L. Berger (World Scientific, Singapore, 1992) p. 134.
- [5] ZEUS Collab., Contributed paper to ICHEP'98, Vancouver, Canada, July 1998, N-812.
- [6] The ZEUS Detector, Status Report (1993), DESY 1993.
- [7] M. Klasen, T. Kleinwort and G. Kramer, *Eur. Phys. Jour. C* **1** (1998) 1.
- [8] B.W. Harris and J.F. Owens, *Phys. Rev. D* **57** (1998) 5555.
- [9] S. Frixione and G. Ridolfi, *Nucl. Phys. B* **507** (1997) 315.
- [10] P. Aurenche, L. Bourhis, M. Fontannaz and J. Guillet, Proc. of “Future Physics at HERA” (1996) 570.
- [11] B.W. Harris, M. Klasen and J. Vossebeld, hep-ph/9905348.

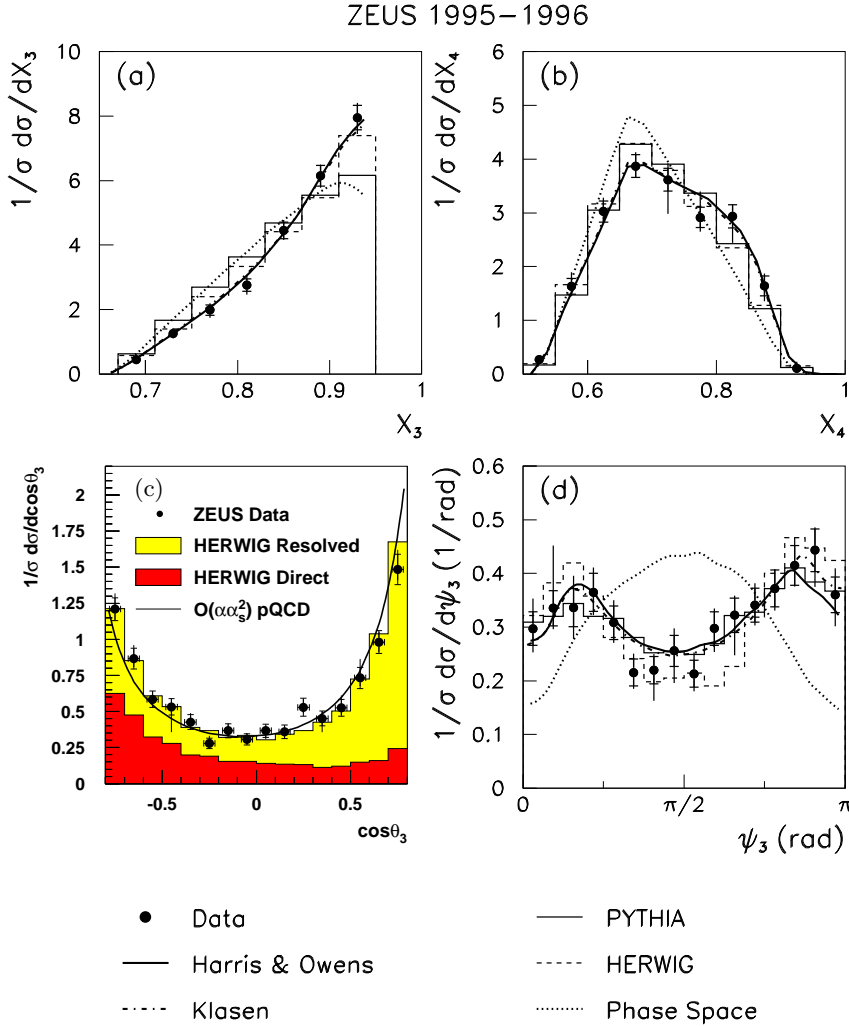


**Figure 13.** (a)  $X_3$  and (b)  $X_4$  distributions, and the angular distributions (c)  $\cos\theta_3$  and (d)  $\psi_3$ .  $\mathcal{O}(\alpha\alpha_s^2)$  and Monte Carlo calculations are shown for comparison.

- [12] L.E. Gordon and J.K. Storrow, *Nucl. Phys. B* **489** (1997) 405.
- [13] M. Glück, E. Reya and A. Vogt *Phys. Rev. D* **46** (1992) 1973.
- [14] P. Aurenche, J.P. Guillet, M. Fontannaz, *Z. Phys. C* **64** (1994) 621.
- [15] H.L. Lai *et al*, *Phys. Rev. D* **55** (1997) 1280.
- [16] ZEUS Collab., J. Breitweg *et al*, *Eur. Phys. Jour. C* **4** (1998) 591.
- [17] S. Catani, Yu.L. Dokshitzer, M.H. Seymour and B.R. Webber, *Nucl. Phys. B* **406** (1993) 187; S.D. Ellis and D.E. Soper, *Phys. Rev. D* **48** (1993) 3160; M.H. Seymour, *Nucl. Phys. B* **513** (1998) 269.
- [18] ZEUS Collab., Contributed paper to IECHEP'99, Tampere, Finland, July 1999, N-530.
- [19] H.-U. Bengtsson and T. Sjöstrand, *Comp. Phys. Comm.* **46** (1987) 43; T. Sjöstrand, *Comp. Phys. Comm.* **82** (1994) 74.
- [20] G. Marchesini *et al*, *Comp. Phys. Comm.* **67** (1992) 465.
- [21] H1 Collab., Contributed paper to IECHEP'99, Tampere, Finland, July 1999, N-157u.
- [22] H1 Collab., I. Abt *et al*, *Nucl. Instr. and Meth. A* **386** (1997) 310 and 348.
- [23] ZEUS Collab., Contributed paper to ICHEP'98, Vancouver, Canada, July 1998, N-805.
- [24] ZEUS Collab., J. Breitweg *et al*, *Phys. Lett. B* **443** (1998) 394.
- [25] M. Klasen, *Eur. Phys. Jour. C* **7** (1999) 225.
- [26] B.W. Harris and J.F. Owens, *Phys. Rev. D* **56** (1997) 4007.

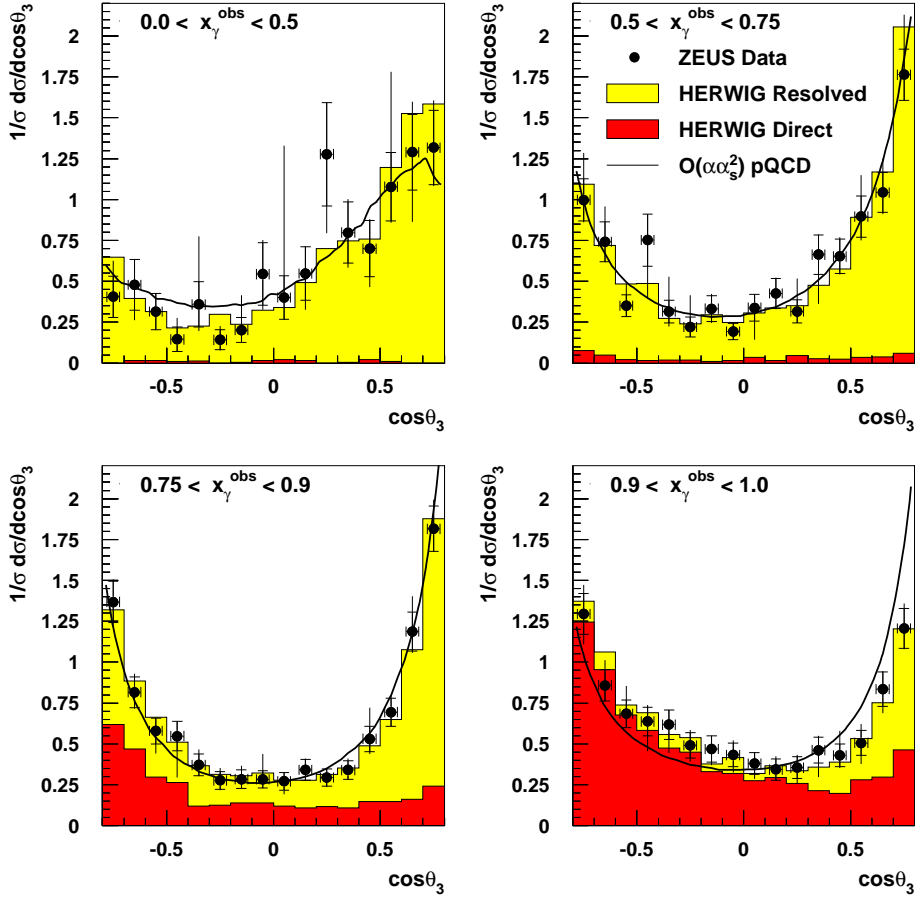


**Figure 14.**  $\cos\theta_3$  distribution.  $\mathcal{O}(\alpha\alpha_s^2)$  and Monte Carlo calculations are shown for comparison.

[27] ZEUS Collab., Contributed paper to IECHEP'99, Tampere, Finland, July 1999, N-544.